Article

NPP-VIIRS DNB Daily Data in Natural Disaster Assessment: Evidence from Selected Case Studies

Xizhi Zhao [1,2,3], **Bailang Yu** [1,2,*], **Yan Liu** [3,*], **Shenjun Yao** [1,2], **Ting Lian** [1,2], **Liujia Chen** [4], **Chengshu Yang** [1,2], **Zuoqi Chen** [1,2] **and Jianping Wu** [1,2]

1   Key Laboratory of Geographic Information Science (Ministry of Education), East China Normal University, Shanghai 200241, China; zhaoxizhizhi@126.com (X.Z.); sjyao@geo.ecnu.edu.cn (S.Y.); Liant93@hotmail.com (T.L.); yjack90824@gmail.com (C.Y.); zqchen@geo.ecnu.edu.cn (Z.C.); jpwu@geo.ecnu.edu.cn (J.W.)
2   School of Geographic Sciences, East China Normal University, Shanghai 200241, China
3   School of Earth and Environmental Sciences, The University of Queensland, Brisbane, Qld 4072, Australia
4   Lab of Spatial Information Integration, Institute of Remote Sensing and Digital Earth, Chinese Academy of Sciences, Beijing 100101, China; chenlj2016@radi.ac.cn
*   Correspondence: blyu@geo.ecnu.edu.cn (B.Y.); yan.liu@uq.edu.au (Y.L.); Tel.: +86-21-5434-1172 (B.Y.); +61-7-3365-6483 (Y.L.)

check for updates

Abstract: Whereas monthly and annual nighttime light (NTL) composite datasets are being increasingly used to estimate socioeconomic status, use of the National Polar-orbiting Partnership Visible Infrared Imaging Radiometer Suite (NPP-VIIRS) Day/Night Band (DNB) daily data has been limited for detecting and assessing the impact of short-term disastrous events. This study explores the application of daily NPP-VIIRS DNB data in assessing the impact of three types of natural disasters: earthquakes, floods, and storms. Daily DNB images one month prior to and 10 days after a disastrous event were collected and a Percent of Normal Light (PNL) image was produced as the ratio of the mean DNB radiance of the pre- and post-disaster images. Areas with a PNL value lower than one were considered as being affected by the event. The results were compared with the damaged proxy map and the flood proxy map generated using synthetic aperture radar data as well as the reported power outage rates. Our analyses show that overall NPP-VIIRS DNB daily data are useful for detecting damages and power outages caused by earthquake, storm, and flood events. Cloud coverage was identified as a major limitation in using the DNB daily data; rescue activities, traffic, and socioeconomic status of the areas also affect the use of DNB daily data in assessing the impact of natural disasters. Our findings offer new insight into the use of the daily DNB data and provide a practical guide for researchers and practitioners who may consider using such data in different situations or regions.

Keywords: NPP-VIIRS; Day/Night Band (DNB) daily data; nighttime light; natural disaster; earthquake; storm; flood

1. Introduction

After a severe natural disaster, quick and effective assessment of the affected areas is vital for post-disaster response and rescue. Traditional methods of disaster assessment largely rely on field survey data [1,2]. However, obtaining survey data is time-consuming and particularly difficult in isolated areas. Remote sensing data offer near real-time and large-scale information about the land surface and have been used widely in disaster assessment. Compared with optical and radar remote sensing data that are mainly used to identify ground deformation or structural damages due to natural disasters [3–6], nighttime light (NTL) remote sensing data can directly reflect human activities because

artificial lights from cities, towns, industrial sites, fishing boats, and other human activities are recorded at night [7,8]. A natural disaster may damage buildings and infrastructure, cause power outages, and reduce human activities, all of which can cause changes in light, which serves as a basis for assessing the impact of natural disasters using NTL data.

There are two commonly used NTL data sources: Defense Meteorological Satellite Program's Operational Line Scan System (DMSP-OLS) and Visible Infrared Imaging Radiometer Suite (VIIRS) Day-Night Band (DNB) onboard the Suomi National Polar-orbiting Partnership (S-NPP) satellite. DMSP-OLS has been acquiring nighttime light imagery since the early 1970s. However, its limitations include coarse radiometric accuracy, low spatial resolution, lack of onboard calibration, and limited dynamic range [9]. The new generation of NPP-VIIRS DNB data provides unprecedented nighttime light observation capability that overcomes some of the limitations in DMSP-OLS images [10]. NPP-VIIRS DNB has a higher radiometric accuracy with onboard calibration and has a specified dynamic range of approximately seven orders of magnitude, from 3×10^{-9} W·cm^{-2}·sr^{-1} to 0.02 W·cm^{-2}·sr^{-1}, which ensures the ability to detect extremely low-level light [11]. NPP-VIIRS DNB data provide global coverage with a 12-h revisit time (at about 1:30 a.m. and 1:30 p.m. local time) and with a spatial resolution of about 750 m throughout the scan.

The yearly or monthly composite NTL data are being increasingly used as an indicator to estimate various socioeconomic indicators such as gross domestic product (GDP) [12–14], population [15,16], poverty [17,18], electric power consumption [19–21], carbon dioxide (CO_2) emissions [22,23], and others [24–27], as well as to evaluate military conflicts [28–30] and to extract urban built-up areas [31,32]. However, the composite NTL data are not suitable for immediate assessment of disasters due to their low temporal resolution. The application of the DMSP-OLS daily images to assessing disasters is limited by the cost of the data and its internal limitations [33]. The NPP-VIIRS DNB daily data are available free of charge, which enables its use in disaster assessment. Daily NTL data from both NPP-VIIRS DNB and DMSP-OLS have been used to detect power outages due to storms and to assess the damage by earthquakes. For example, Elvidge et al. [34] overlaid the daily NTL image after Hurricane Fran with the reference data of stable lights from DMSP-OLS data to form a color composite image and visually identify areas with power outages; Molthan et al. [35] produced a false-color composite image of pre- and post-hurricane nighttime light from daily NPP-VIIRS DNB data to detect changes in light and identify areas with possible power outages. Cole et al. [36] differentiated the pre- and post-hurricane nighttime light imagery based on the NPP-VIIRS DNB to produce a Percent of Normal Light (PNL) image and developed a neural network model to detect power outages. Cao et al. [37] used a time-series mean NPP-VIIRS DNB radiance to estimate the light outage and Wang et al. [38] used the National Aeronautics and Space Administration (NASA) Black Marble nighttime light data (a type of high-quality NTL data derived from NPP-VIIRS DNB) and PNL to assess disaster-related power outages. Similarly, Kohiyama et al. [39] and Hayashi et al. [40] used the histogram of the digital number (DN) difference between the pre- and post-earthquake DMSP-OLS images to identify damaged areas. Fan et al. [41] used NPP-VIIRS Nearly Constant Contrast (NCC) nighttime light, derived from NPP-VIIRS DNB data, to detect damage after three earthquakes. NTL daily data have also been used to detect holiday events and wars. For instance, Roman et al. [42] used time series data of the total lighting electricity usage (TLEU), estimated from daily NPP-VIIRS DNB, for several cities in the Southern United States, Northern Mexico, and the Middle East to detect the energy usage during the Christmas–New Year period and the Holy Month of Ramadan. Agnew et al. [43] compared four DMSP-OLS nighttime light images in Baghdad before and after the U.S. military 'surge', to assess the extent to which nighttime lights changed after the war. The most commonly used methods to detect NTL changes include pixel-based pre- and post-event image comparison [34–36,38–41,43], and region-based time series analyses [37–39,42].

Several studies used NTL daily data to assess the impact of disasters. However, few research articles have compared the use of such data across different types of disasters. Given the distinct characteristics of each type of natural disaster that would differently affect NTL, it is necessary to

evaluate the usefulness and limitations of this source of data when assessing the impact of different types of natural disasters. It is also necessary to understand the difference between the use of NTL and radar data in this context, given that NTL data detect human lights whereas radar data detect ground deformation.

This paper analyses the usefulness and limitations of using NPP-VIIRS DNB daily observations when assessing the impact of several types of natural disasters, including earthquakes, storms, and floods. We aimed to provide a practical guide for researchers and practitioners who may consider using these data sources in different situations or regions. Specifically, we generate a PNL image to present the DNB change before and after a disaster, evaluate the change in space, and explore possible reasons for the change. By examining the usefulness and limitations of the data when assessing the impact of each type of disaster, their implications are evaluated and discussed. We also evaluate and compare the differences between using DNB and radar data in detecting the effects of natural disasters. The remainder of this study is organized as follows. Section 2 describes the selection of the three types of disastrous events as well as data and methods used in this study. Sections 3 and 4 present the results and discussion, respectively. Conclusions are summarized in Section 5.

2. Materials and Methods

2.1. Event Selection

According to the Emergency Events Database (EM-DAT) launched by the Centre for Research on the Epidemiology of Disasters (CRED) of the U.S., the top 10 types of major natural hazards in the world ranked by the number of deaths since 1900 are: drought, epidemic, floods, earthquakes, storms, extreme temperature, volcanic activity, landslides, fog, and wildfire [44]. In this study, we selected three major disaster types: floods, earthquakes, and storms. We did not attempt to assess other types of disasters because droughts, epidemics, extreme temperatures, and fogs are not likely to directly cause NTL reduction; volcanic activity and wildfire are accompanied by serious smoke; and landslides typically happen in undeveloped mountainous areas with little light. For each of the three types of disasters, we selected two typical disastrous events that had significant impacts on people. The study areas contained the most affected areas in these disasters. As the daily NPP-VIIRS DNB data have only been available since 18 July 2012, we selected disasters after this date. Table 1 lists the basic information of the disaster events that were selected and Figure 1 illustrates the locations and land cover categories of each study area.

Table 1. The selected disaster events and study area.

Disaster Type	Event	Time	Study Area
Earthquake	Gorkha Nepal Earthquake	25 April 2015 06:11 a.m. (UTC)	Kathmandu and the surrounding area (Area size: 48 km × 57 km), Nepal
	Central Italy Earthquake	24 August 2016 01:36 a.m. (UTC)	Accumoli, Amatrice, Norcia, and Arquata Del Tronto, Italy
Storm	Hurricane Maria	20 September 2017 10:15 a.m. (UTC)	Puerto Rico, U.S.
	Tropical Cyclone Hudhud	12 October 2014 04:30 p.m. (UTC)	Visakhapatnam, India
Flood	Louisiana Flood	11 August 2016–16 August 2016	East Baton Rouge Parish and Livingston Parish, U.S.
	Yulin Flood	25 July 2017–26 July 2017	Suide, China
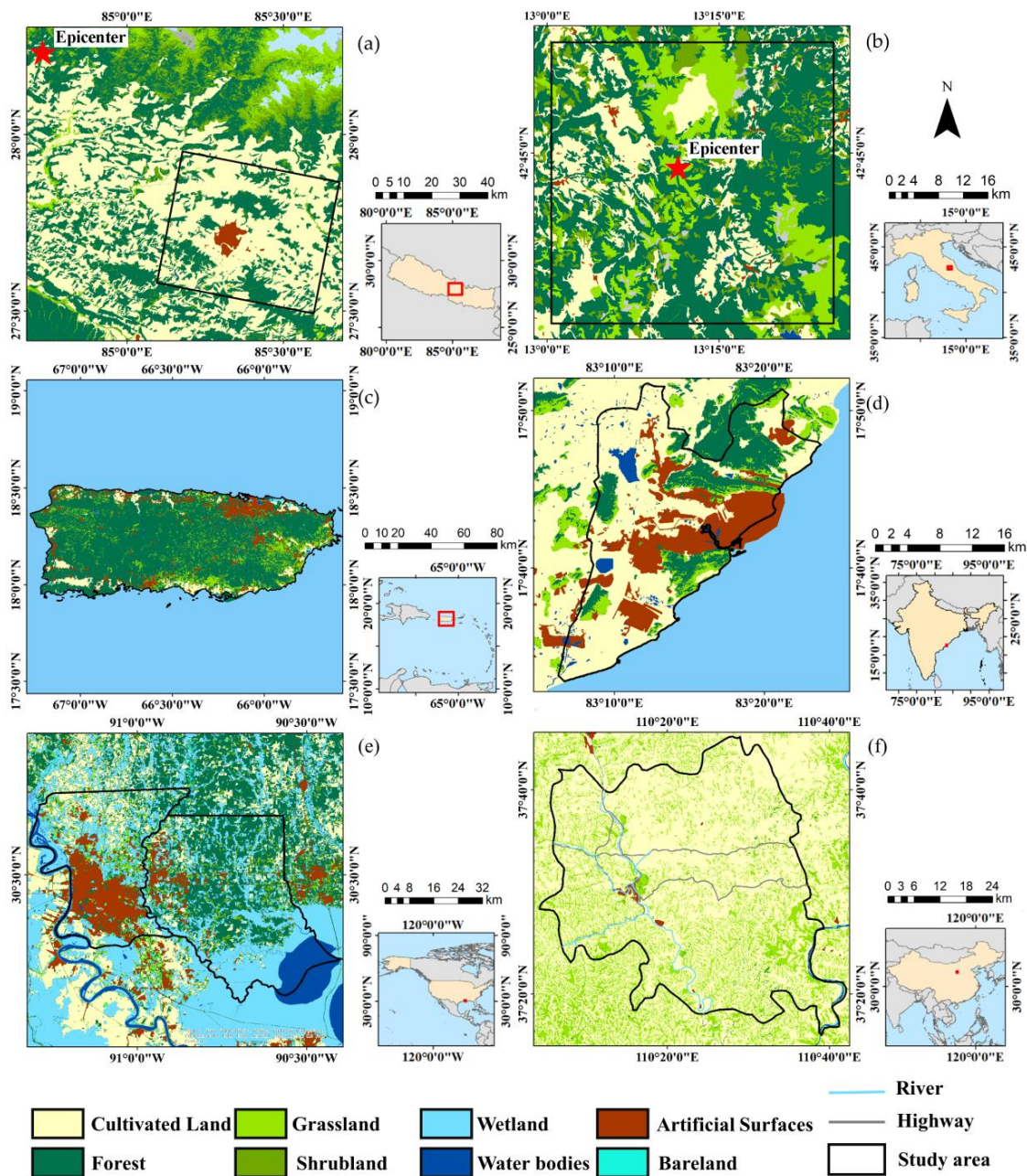
Figure 1. The location and land cover categories from the National Geomatics Center of China of each study site of the six disaster events: (**a**) Gorkha Nepal Earthquake, (**b**) Central Italy Earthquake, (**c**) Hurricane Maria, (**d**) Tropical Cyclone Hudhud, (**e**) Louisiana Flood, and (**f**) Yulin Flood.

The Gorkha Nepal Earthquake in 2015 had a magnitude of 7.8 and caused 8790 deaths and 22,300 injuries in Nepal [45]. The epicenter was in Barpak, Gorkha district (Figure 1a) and it had a depth of 15 km [2]. The study area contains Kathmandu (the capital of Nepal), Bhaktapur, and parts of Nuwakot, Sindhupalchok, Kavrepalanchok, Lalitpur, Makwanpur, and Dhading. The earthquake caused 1222 deaths in Kathmandu, 333 deaths in Bhaktapur, and a large number of houses in the areas to collapse [45].

The Central Italy Earthquake in 2016 was a 6.2 magnitude earthquake that hit central Italy. Although it had a lower magnitude than the Gorkha Nepal Earthquake, it had a shallower epicenter depth of 4.4 km causing more violent ground shaking. The study area contains the four worst-affected counties in Central Italy: Accumoli (epicenter), Amatrice, Norcia, and Arquata Del Tronto. According to the news report [46], 80% of the old town center in Amatrice was destroyed and almost every building

was cracked. As of 26 August 2016, the earthquake had caused 297 deaths with 234 in Amatrice, 11 in Accumoli, and 49 in Arquata del Tronto [47].

Hurricane Maria was the strongest storm that attained landfall in Puerto Rico in the past 85 years. It hit Puerto Rico as a Category 4 hurricane with a maximum sustained wind of 249 km/h, resulting in catastrophic damage and a large scale power outage across the whole island [48]. More than 3 million people were affected by the event [49]. As of 21 September 2017, 100% of the island was without power, and only 20% of these areas were reconnected with power one month after the hurricane [50].

Tropical Cyclone Hudhud was a Category 4 storm with a maximum sustained wind speed of 217 km/h that made landfall at Visakhapatnam [51]. A maximum storm surge of 1.4 m above astronomical tide was reported [52]. The sustained winds and storm surge broke electric poles throughout almost the entire city and destroyed some switching stations, resulting in a lengthy power outage in most parts of Visakhapatnam [53].

Louisiana Flood was caused by upper-level low-pressure weather that brought heavy rainfall of 50 to 80 cm to Southeast Louisiana and Southwest Mississippi from 11 to 13 August 2016. This deluge caused rivers to overflow and resulted in catastrophic flooding and affected large portions of the highly populated East Baton Rouge, Livingston, Ascension, and Tangipahoa Parishes [54]. On the night of the 15 August, about 14,300 Entergy (an electric distribution utility company in Louisiana) customers in East Baton Rouge Parish and Livingston Parish were out of power [55]. In addition, 75% of the homes in Livingston Parish were reported as a 'total loss' [56].

For the Yulin Flood, from 6:00 p.m. on 25 July to 6:00 a.m. on 26 July 2017, a heavy rain event hit Yulin City in Shaanxi Province, China. The induced flood inundation of 12 counties included Suide, which was reported as one of the most affected counties. The maximum precipitation in Suide was 103.4 mm [57]. According to the report by the China National Commission for Disaster Reduction, in Suide County alone, the flood had caused 6 deaths, 86 injuries, 194 households to experience house collapse, 61 bridges to collapse, and 213 roads to be damaged [58].

2.2. Data

Two types of NPP-VIIRS data were utilized for this study: the DNB Sensor Data Record (SDR) and the Cloud Cover Layer (CCL) Environmental Data Record (EDR). The DNB SDR provides radiance and the corresponding geolocation data (including longitude, latitude, height, and lunar zenith angle). The DNB radiance was used to quantify light emission from artificial light. The geolocation data were used for lunar radiance removal and edge-of-swath pixel discarding in the data preprocessing process. CCL data provided information on cloud cover fraction and were used to filter out the DNB contaminated by cloud. These NPP-VIIRS data were retrieved from the National Oceanic and Atmospheric Administration (NOAA)'s Comprehensive Large Array-data Stewardship System (CLASS) [59].

The Moderate Resolution Imaging Spectroradiometer (MODIS) Terre V005 500 m Surface Reflectance product (MCD09A1) was used as auxiliary data to quantify the reflected lunar radiance observed by the DNB sensor. MODIS data are available through the EARTHDATA website powered by the Earth Observing System Data and Information System (EOSDIS) [60].

The Damage Proxy Maps (DPMs) and Flood Proxy Maps (FPMs) produced under the NASA Advanced Rapid Imaging and Analysis (ARIA) Project [61] were used for validation and for comparison with the affected area detected by NTL. The DPM was generated using an algorithm that detects damage by comparing deformation of land structures using pre- and post-disaster X-band interferometric synthetic aperture radar (SAR) data from the Italian Space Agency's COSMO-SkyMed (CSK) satellite constellation. It has a resolution of about 30 m. The FPM was derived from ALOS-2 ScanSAR data and has a resolution of about 50 m.

We used building range maps from Open Street Map (OSM) [62] to extract building footprints. Land Cover Maps for each event site, at a 30-m resolution for 2010, acquired from the National

Geomatics Center of China [63], were also used to represent surface coverage type. Administrative boundary data were obtained from the Global Administrative Areas (GADM) database [64].

2.3. Methods

We first processed the raw images to remove lunar radiance, cloud, and edge-of-swath pixels. PNL images were then generated from the processed images to detect areas that had been affected by the disastrous events.

2.3.1. Data Preprocessing

NPP-VIIRS DNB captures light from city lights, fishing boats, fire, gas flares, lighting, auroras, volcanic magma, as well as reflected moonlight from clouds, snow cover, and the ground [10]. The data quality is affected by stray light and the position of the pixels in the swath [65]. To correctly detect human-related light changes after natural disasters, preprocessing work was required. For our selected case study events, we performed lunar radiance removal, cloud clearing, and edge-of-swath pixel removal as the other conditions such as fishing boats, gas flares, lighting, auroras, volcanic magma, and stray light were not in effect. Figure 2a shows a DNB image free from the impact of these factors. Figure 2b–e shows DNB images affected by moonlight, cloud, moonlight and cloud, and at the edge of the swath, respectively. The methods we applied to achieve this are described below.
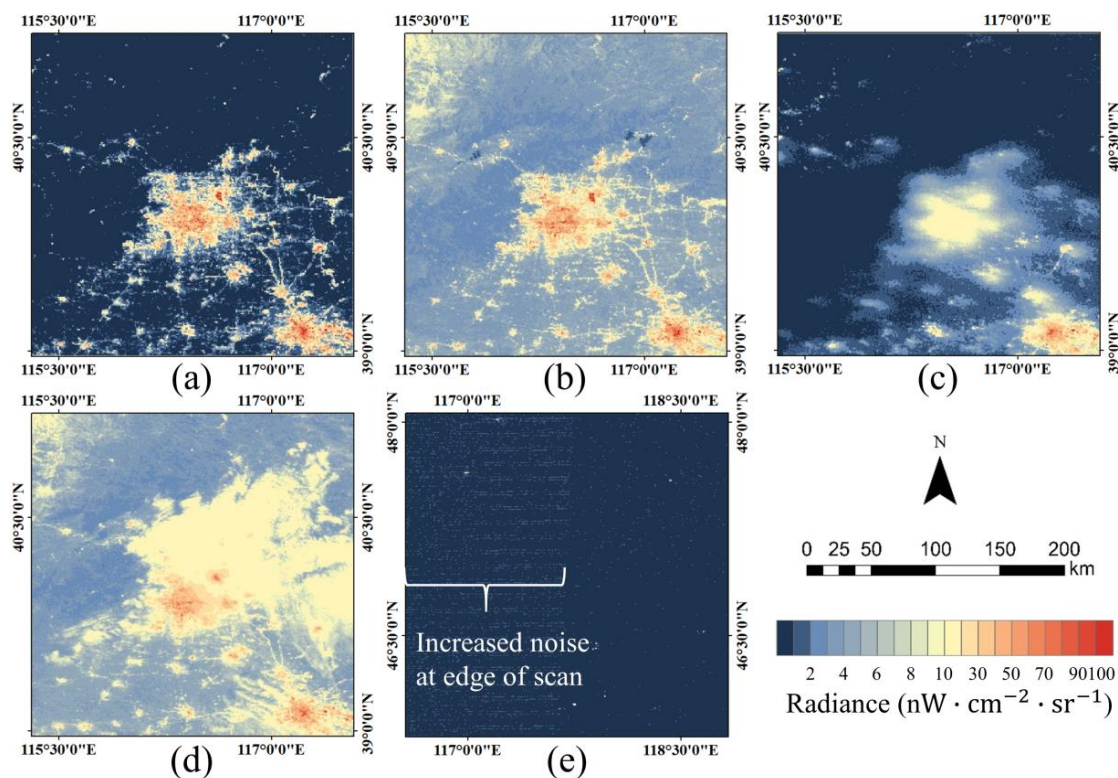
Figure 2. National Polar-orbiting Partnership Visible Infrared Imaging Radiometer Suite (NPP-VIIRS) Day/Night Band (DNB) images under different conditions: (**a**) no moonlight or cloud, (**b**) moonlit, (**c**) cloudy, (**d**) moonlit and cloudy, and (**e**) edge-of-swath.

For cloud-free observations, DNB nighttime imagery is a composition of light emissions and the reflected moonlight from cloud tops and land surfaces [36,37,66]. The DNB can capture moonlight when the moon is above the horizon at the satellite overpass time for about 15 days in a lunar cycle (about 29.5 days) [8]. The DNB radiance of a place under full moon conditions could be three times larger than the radiance under a noon moon condition [67]. Therefore, the lunar radiance should be removed to determine the true light radiance.

The amount of moonlight reflected from the earth's surface depends on the lunar phase (ranging from new to full moon), elevation, azimuth, and the surface reflectance. Cao [37] introduced a method to compute the lunar radiance observed by DNB sensors with the assistance of a Top of Atmosphere (TOA) spectral lunar irradiance model (MT2009) developed by Miller and Turner [68]. We adapted this method by using 8-day MODIS surface reflectance instead of TOA reflectance to quantify the lunar radiance contribution to produce the lunar-corrected nighttime light data.

To compute the lunar radiance (L_m), as observed by the DNB sensor, we used:

$$L_m = \frac{E_m}{\pi} \rho \cos(\theta_m) \tag{1}$$

where θ_m is the lunar zenith angle provided by NPP-VIIRS DNB SDR, E_m is the downwelling TOA sensor response function-weighted lunar irradiance derived from the MT2009 model, and ρ is the band averaged surface reflectance and is estimated using Band 1, 2, and 4 channels of MOD09A1. The true light radiance is the initial DNB radiance subtracting the lunar radiance L_m.

Clouds have a complex effect on DNB images according to the opacity of the cloud and the intensity of the moonlight. In no-lunar-illumination conditions, clouds can block the city light below them and blur the surrounding lights (Figure 2c). However, in high-lunar illumination conditions, clouds not only dim the city light but also reflect moonlight (Figure 2d). The Summed Cloud Cover (SCC) from the NPP-VIIRS CCL data have been proven to have good ability to detect clouds [69]. SCC is the cloud fraction summed over all layers and has a range from 0 to 1. A pixel with an SCC equal to 0 indicates that the pixel is clear of cloud. A strict criterion for SCC values smaller than 0.01 was used to identify and exclude the cloud-contaminated pixels.

The DNB covers the earth with a swath width of 3044 km. To achieve a near-constant 742 m sample, the swath was aggregated into 32 zones on each side of the nadir via a scan-angle-dependent aggregation strategy [70]. The last four aggregation zones (zone 29–32) at the edge of the scan have a visible increase in noise [36] (Figure 2e), so that pixels in these zones were discarded.

A manual process was conducted to visually assess the image of each date in order to identify and exclude images that may have obvious problems, such as being affected by heavy aerosol or clouds that may not be detected using the SCC measure.

2.3.2. PNL Image

The NPP-VIIRS DNB data one month prior to and 10 days after the natural disaster (excluding images with poor data quality) were averaged to create pre- and post-disaster composite datasets, respectively. This method was necessary for two reasons. Firstly, most missing data caused by clouds could be removed by averaging the images over the selected period. Secondly, the intensity of city lights observed by satellites can fluctuate due to many factors such as atmospheric scattering and absorption [39] and differences in scan angle [65]. By averaging the data, these fluctuations could be smoothed and the data would reflect the real light. We chose a relatively longer pre-disaster period (one month) to smooth the normal time fluctuations and reflect the real light during normal conditions. A shorter 10-day post-disaster period was chosen, as this is the critical period that reflects the changing conditions before recovery work occurs. Seasonal effects of NTL data caused by changes in NDVI, snow, and albedo [71] were negligible due to the minimal change in these factors during this short time period. A PNL image was used to compare the DNB images pre- and post-disasters. PNL was calculated for each pixel by dividing the post-disaster composite data by the pre-disaster composite data. This approach follows previous work by Cole et al. in assessing power outages [36], which is calculated as:

$$PNL = 100 \times \left(\frac{Rad_{post}}{Rad_{pre}} \right) \tag{2}$$

where Rad_{post} is the post-disaster composite DNB radiance and Rad_{pre} is the pre-disaster composite DNB radiance. PNL can reflect changes of lights before and after the disaster, where a PNL > 1 means more light after the disaster, PNL < 1 means less light after the disaster, and PNL = 1 means no changes.

The areas where PNL < 1 were viewed as the disaster-affected areas. However, when the Rad_{pre} and/or Rad_{post} values are very small, any small change in DNB radiance due to background noises in an areas [10] can result in an extremely high or low PNL value using Equation (2), which would be unacceptable. To avoid this situation, we reset all Rad_{pre} and Rad_{post} values to 0.3 nW·cm^{-2}·sr^{-1} when the actual value was lower than this threshold. This threshold was chosen empirically, whereas either lower or higher than this threshold resulted in large anomalies in the PNL.

2.3.3. Statistical Significance

The Mann-Whitney U-test was used to test the statistical significance of the DNB changes at the pixel level. The Mann-Whitney U-test is a nonparametric test that tests for differences between two independent groups with no specific distribution [72]. As the DNB values of the study areas were not normally distributed, the Mann-Whitney U-test was suitable for comparisons between them. The Mann-Whitney U-test has been used to compare the nighttime light before and after a war [43]. The null hypothesis (H0) stipulates that the two groups of data are homogeneous and have the same distribution, whereas the alternative hypothesis (H1) stipulates that the distributions of the two groups are different [72]. This study tested the statistical significance of DNB changes using a 95% confidence interval. So, if the *p*-value was smaller than 0.05, the H0 was rejected, meaning that the difference between the pre-and post-disaster DNB images was statistically significant.

3. Results

3.1. Earthquakes

The first earthquake we analyzed was the Gorkha Nepal Earthquake. Table 2 lists the dates and cloud coverages of pre-and post-earthquake DNB images that were used to compute the average composite DNB images pre- and post-earthquake (Figure 3a,b). Figure 3c shows the PNL image. Green indicates areas with a PNL less than one, and these were considered to be zones damaged by the earthquake. Both the extent and intensity of the light in most areas were reduced after the earthquake, with only a few exceptions. The size of the areas that became darker after the earthquake was calculated to be 447.2 km^2 and the size of those that became brighter was calculated to be 145.1 km^2. Using the Mann-Whitney U-test, the DNB changes post-earthquake were statistically significant at $p < 0.001$.

Table 2. The dates and cloud coverages of pre- and post-earthquake Day/Night Band (DNB) images of the Gorkha Nepal Earthquake in 2015.

Date	Pre-Earthquake						Post-Earthquake			
Date	7April	8 April	9 April	18 April	21 April	23 April	26 April	2 May	4 May	5 May
Days Before (After) the Disaster	18	17	16	7	4	2	1	7	9	10
Cloud Coverage (%)	0.1	0.0	0.0	0.7	0.6	2.5	17.1	1.1	1.1	0.1
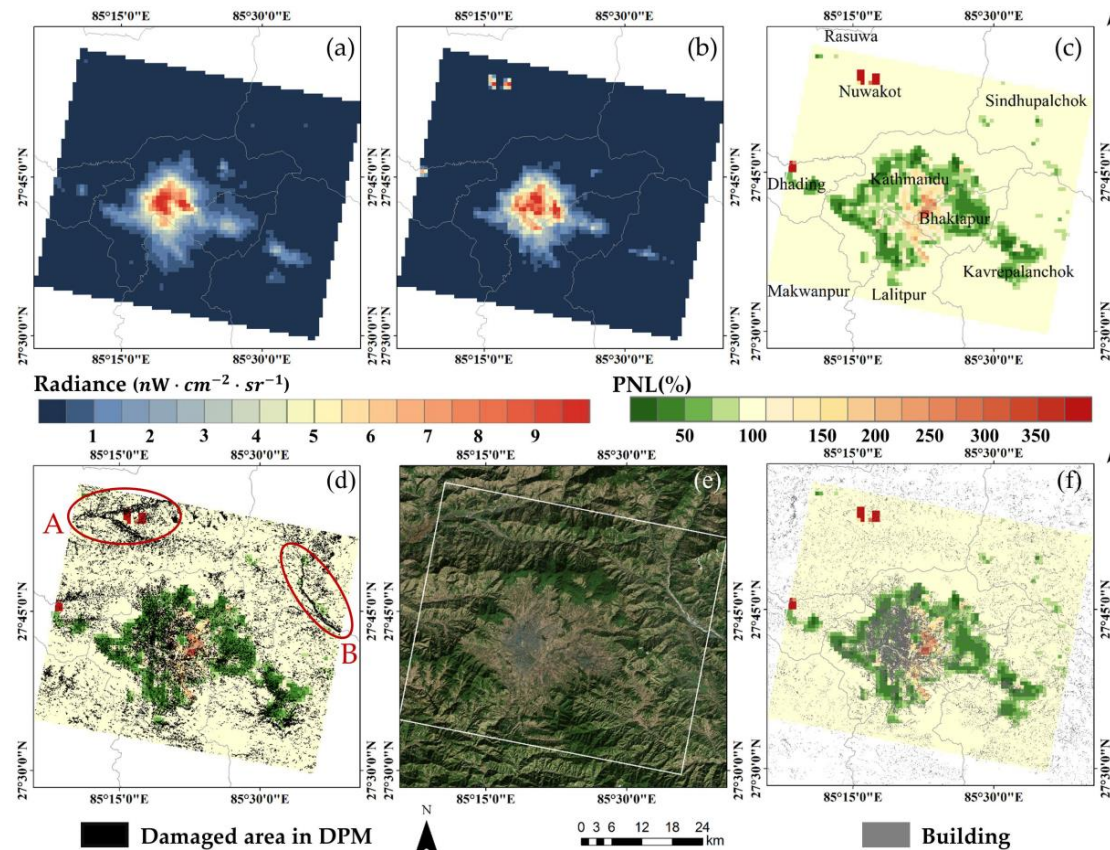
Figure 3. (**a**) The pre- and (**b**) post-earthquake averaging composite DNB images, (**c**) Percent of Normal Light (PNL) image, (**d**) Damage Proxy Map (DPM) image combined with PNL image, (**e**) Bing satellite map, and (**f**) Open Street Map (OSM) building map combined with PNL image of the Gorkha Nepal Earthquake.

We compared the results to DPMs generated using SAR data from CSK. Figure 3d shows the PNL image overlaid by the damaged areas (marked as black pixels) from DPM. The damaged areas in the PNL and DPM images concur with each other in the particular area of central Kathmandu. However, the damaged areas in DPM image are denser in regions A and B where there is no noticeable change in NTL (Figure 3d). By comparing Figure 3d with the Bing satellite map (Figure 3e), we found that region A is a mountainous area and that there is a river in region B. The mountain deformation and river changes created by the earthquake were detected by the SAR data. By comparing the PNL and DPM images with the building map derived from the OSM (Figure 3f), we found that many of the damaged areas detected by radar data were located in areas with no buildings or low building density, whereas damaged areas derived from the NTL were almost all located in central Kathmandu with high building density.

To assess the accuracy of using NTL to detect the damage due to earthquakes, we reduced the resolution of the DPM from 30 m to 750 m to match the resolution of the PNL image for comparison. A confusion matrix was constructed (Table 3) that shows an overall accuracy of 75.5%. A True Positive Rate (TPR) of 35.9%, and a False Positive Rate (FPR) of 8.9% indicate that 35.9% of the damaged areas and 8.9% of the undamaged areas were detected as damaged areas. Given that the proportion of the undamaged area was much larger than that of the damaged area, we further calculated the standard Kappa ($K_{standard}$) as well as Kappa for location ($K_{location}$) and quantity ($K_{quantity}$) using Pontius' approach [73]. $K_{location}$ was calculated by dividing the success due to the model's ability to specify location by the maximum possible success due to a model's ability to specify location perfectly given a fixed quantity of each class, which measures the locational agreement between two maps. $K_{quantity}$ was calculated by dividing the success due to the model's ability to specify quantity by the

maximum possible success due to a model's ability to specify quantity perfectly given a fixed $K_{location}$, which measures the agreement in the quantity of the two maps. Kappa values range from -1 (no agreement) to 1 (perfect agreement), where positive values show a greater agreement than usual. A $K_{standard}$ of 0.31 indicates that the damaged areas detected by NTL and DPM have fair agreement overall. A $K_{location}$ of 0.46 and a $K_{quantity}$ of 0.82 indicate that the PNL has a moderate ability to specify the location of damage and a good ability to specify the quantity of damage, respectively.

Table 3. The confusion matrices and accuracy for using nighttime light (NTL) images to detect areas of damage after earthquake events.

Earthquake Event	Actual (DPM)	Predicted (NTL)			Accuracy
		Damaged	**Undamaged**	**Total**	
Gorkha Nepal Earthquake	Damaged	488 (35.9%)	871 (64.1%)	1359	Overall accuracy = 75.5% TPR = 35.9% FPR = 8.9% $K_{standard}$ = 0.31 $K_{quantity}$ = 0.82 $K_{location}$ = 0.46
	Undamaged	307 (8.9%)	3150 (91.1%)	3457	
	Total	795	4021		
Central Italy Earthquake	Damaged	5 (12.5%)	35 (87.5%)	40	Overall accuracy = 90.2% TRP = 12.5% FPR = 9.0% $K_{standard}$ = 0.01 $K_{quantity}$ = 0.84 $K_{location}$ = 0.04
	Undamaged	322 (8.9%)	3298 (91.1%)	3620	
	Total	327	3333		

We noticed that a large proportion of the damaged area became brighter after the earthquake and the brighter areas were mostly located in central Kathmandu (Figure 3f). This was probably due to rescue and recovery activities. According to the Ministry of Home Affairs (MoHA) of Nepal, over 130,000 staff from the Nepal Army, Nepal Police, Armed Police Force, as well as 4000 government and private health workers participated in the rescue activities [45]. Rescue and recovery activities from badly damaged buildings, repairing damaged infrastructure, and building temporary houses for displaced people would require a large number of emergency lights [74], resulting in the brighter color on the image. Figure 3f shows that the darker areas were mainly located in suburban or rural areas, whereas brighter areas were mainly located at the urban center, indicating that the urban center may have received more relief than the suburban and rural areas.

Assessment of the Central Italy Earthquake in 2016 was based on DNB images listed in Table 4. Figure 4a–c shows the pre- and post-earthquake DNB and PNL images for the four counties in Italy. The difference between the pre- and post-earthquake DNB images was statistically significant (Mann-Whitney U-test, $p < 0.001$).

Table 4. The dates and cloud coverages of pre- and post-earthquake DNB images of the Central Italy Earthquake.

	Pre-Earthquake									Post-Earthquake			
Date	4 August	5 August	8 August	9 August	11 August	12 August	13 August	14 August	15 August	26 August	27 August	28 August	30 August
Days Before (After) the Disaster	20	19	16	15	13	12	11	10	9	2	3	4	6
Cloud Coverage (%)	5.5	4.6	4.0	12.3	0.0	0.0	2.1	15.6	21.9	4.0	16.1	0.0	0.0
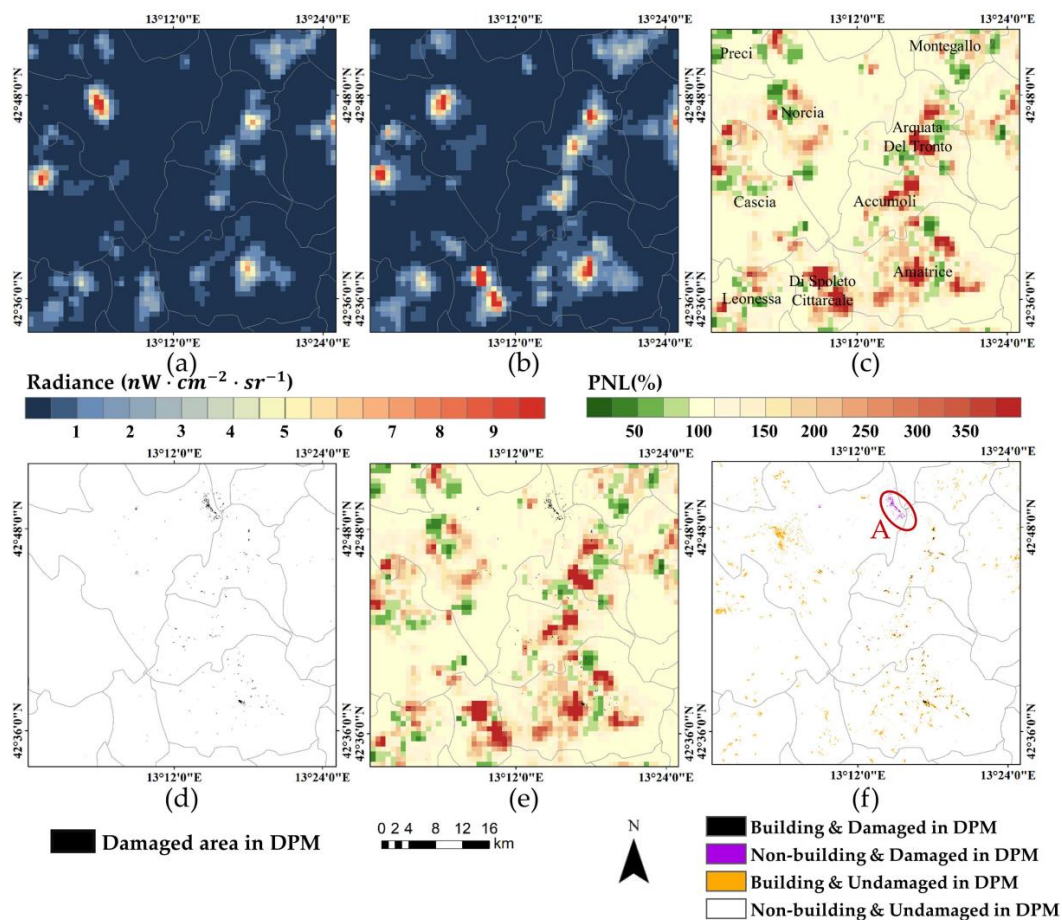
Figure 4. (**a**) The pre- and (**b**) post-earthquake averaging composite DNB images, (**c**) PNL image, (**d**) DPM image, (**e**) DPM image combined with PNL image,; and (**f**) DPM image compared with OSM building map of the Central Italy Earthquake.

Unlike the Gorkha Nepal Earthquake and other previous studies [39,40], the area of brighter pixels (900.6 km^2) was far larger than that of darker pixels (183.9 km^2). The average DNB radiance increased after the earthquake from 0.54 nW·cm^{-2}·sr^{-1} to 0.76 nW·cm^{-2}·sr^{-1}, which could be attributed to rescue and recovery activities. Comparing the PNL image with the DPM (Figure 4d,e) produced by ARIA using CSK SAR data, most damaged areas were brighter after the earthquake. By comparing the DPM image with the building map (Figure 4f), we found that most damaged areas detected by DPM were districts where buildings were present, except for the mountainous region A where there were no buildings but land deformation occurred. The overall accuracy was high (90.2%), whereas the TRP was only 12.5% and the standard Kappa was extremely low (0.01) (Table 3, Row 2), indicating that it was not possible to use PNL to detect damaged areas. The overall accuracy was high simply because the undamaged area was much larger than the damaged area.

The difference in light change patterns between the Gorkha Nepal Earthquake and the Central Italy earthquake is possibly attributable to their different population, building, and economic conditions. In Italy, these small towns were quiet and peaceful with few people or nighttime activities. When the earthquake occurred, rescue teams entered the affected areas with emergency lights [75,76], resulting in the town being even brighter than during normal time. However, in Nepal, the population of the study area was 380 times larger than that of the study area in Italy, the number of buildings was 18 times larger, and the average number of people per building was 20 times larger (Table 5). After the earthquake, the number of damaged buildings was so large that the rescue teams could not reach every building in time. Thus, the rescue lights were not able to complement the decreased light caused by earthquakes.

Table 5. The building numbers and population in the study areas of the two earthquake events.

Study Area	Number of Buildings [1]	Total Population [2]	Average Number of People Per Building
Kathmandu and the surrounding area, Nepal	220,451	3,566,322	16.2
Four counties in Italy	12,234	9371	0.8

[1] The number of buildings was calculated from the OSM building map in the study areas. [2] The total population was extracted from the Gridded Population of the World (GPW) dataset, v4. (http://sedac.ciesin.columbia.edu/data/collection/gpw-v4).

3.2. Storms

For Hurricane Maria, we used seven DNB images prior to the storm and five images after the storm (Table 6) to compute the average composite DNB images pre- and post-storm. Hurricane Maria occurred during the rainy season during very high average cloud coverage of 85.0% within the first 10 days after the hurricane. As such, we were unable to use NTL these days. Given that 84% of the island was still without power 20 days after the hurricane [50], we averaged the DNB for 20 days after the hurricane as the post-storm data. Figure 5a–c show the pre- and post-storm averaging composite DNB images and the PNL image. Most areas of the island were darker after the hurricane, with only a few exceptions. The size of the darker areas was calculated to be 9581.6 km^2 and the brighter areas were only 53.4 km^2. The DNB changes post-earthquake were statistically significant (Mann-Whitney U-test, $p < 0.001$).
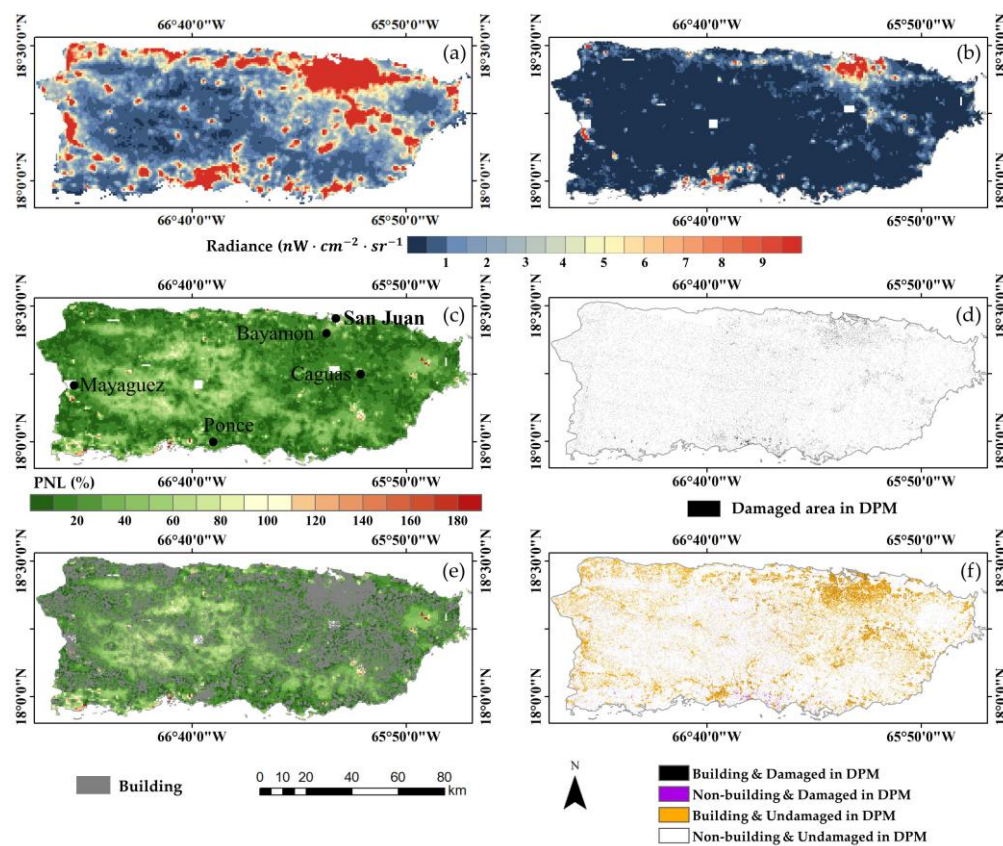

Figure 5. (**a**) The pre- and (**b**) post-storm averaging composite DNB images, (**c**) PNL image, (**d**) DPM image, (**e**) OSM building map combined with PNL image, and (**f**) DPM image compared with the building map of Hurricane Maria.

Table 6. The dates and cloud coverages of pre- and post-storm DNB images of Hurricane Maria.

	Pre-Storm							Post-Storm				
Date	22 August	23 August	24 August	28 August	30 August	1 September	18 September	27 September	28 September	29 September	7 October	8 October
Days Before (After) the Disaster	29	28	27	23	21	19	2	7	8	9	17	18
Cloud Coverage (%)	15.2	8.1	11.4	11.1	19.9	19.7	20.3	41.2	71.8	48.2	70.8	34.4

By comparing the PNL image (Figure 5c) with the damaged areas from DPM (Figure 5d) produced by ARIA using CSK SAR data, we found that the damaged areas in DPM were sporadic and the extent of the damaged area was lesser than that of the darker area detected by NTL. By overlaying the DPM map with the building map (Figure 5f), we calculated that only 1.6% of the total building areas were affected by Hurricane Maria. This proportion of building damage was significantly less than the proportion of darker pixels (99.4%), indicating that the building damage was not reflected by NTL in this case. This could possibly be attributed to the large-scale power outages resulting in the darkening of both damaged and non-damaged buildings, as well as areas where no buildings were present (Figure 5e). We used the power outage data from the Hurricanes Event Summary Reports published by the U.S. Office of Cybersecurity, Energy Security, and Emergency Response (CESER) to verify the use of PNL to track power outages and recovery trends [50]. These reports provide data about the percent of customers without power ($P_{nopower}$) for 45 days in Puerto Rico for the period from 20 September to 6 November 2017 and from 3 January to 4 April 2018. Using a piecewise linear interpolation, we estimated the $P_{nopower}$ for the other days during this period except for the period from 7 November 2017 to 2 January 2018 where no data were available for this period. We composited the DNB data every 10 days after the storm (except for the period where no $P_{nopower}$ data were available), then selected the composite images not affected by clouds to calculate the PNL value for the whole island by dividing the mean post-storm DNB radiance by the mean pre-storm DNB radiance (Table 7). The $P_{nopower}$ values for the selected days were averaged and used as validation data (Table 7). The average DNB radiance and PNL value for the composite image increased as the $P_{nopower}$ decreased. A linear regression analysis showed that the correlation coefficient (R^2) between PNL and $P_{nopower}$ was 0.94 (Figure 6).
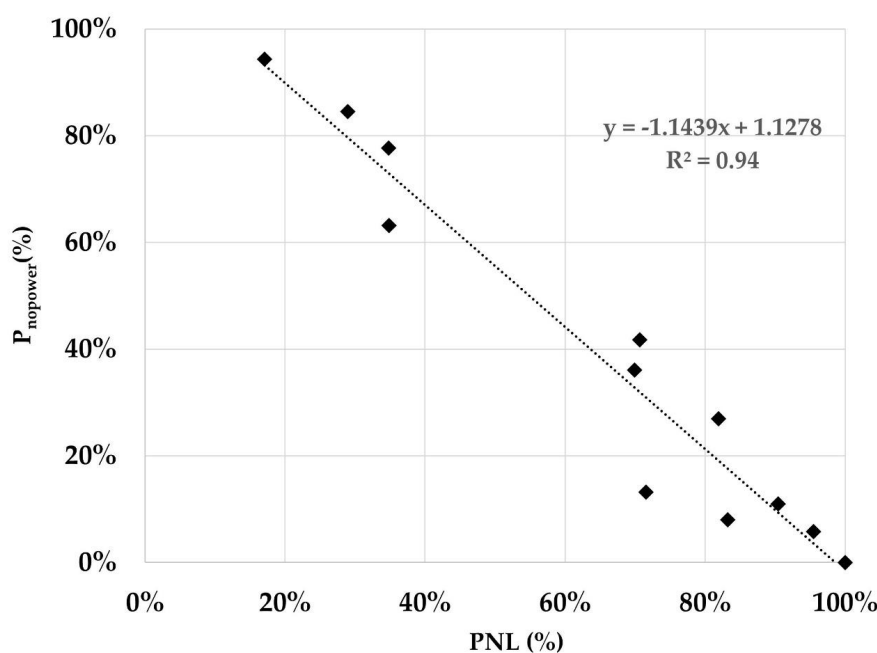
Figure 6. The correlation between PNL and the percent of customers without power ($P_{nopower}$) in Puerto Rico.

Table 7. The PNL and the percent of customers without power ($P_{nopower}$) values of Puerto Rico after Hurricane Maria.

|	Date Range	Dates of Available Image	Average DNB nW·cm^{-2}·sr^{-1}	PNL	$P_{nopower}$
Before Storm	20 August –20 September	22 August–24 August, 28 August, 30 August, 1 September, 18 September	4.52	0.0%	0.0%
After Storm	21 September –10 October	27 September –29 September, 7 October, 8 October	0.77	17.1%	94.3%
	11 October –20 October	13 October, 15 October, 18 October, 19 October	1.31	29.0%	84.5%
	21 October –30 October	22 October –27 October	1.57	34.8%	77.7%
	31 October –9 November	31 October, 1 November, 3 November, 4 November	1.58	34.9%	63.1%
	03 January –12 January	3 January, 4 January, 10 January	3.20	70.7%	41.7%
	13 January –22 January	13 January –15 January, 18 January, 21 January, 22 January	3.16	69.9%	36.0%
	23 January –1 February	4 February, 9 February, 10 February, 11 February	3.70	81.9%	26.9%
	22 February –3 March	22 February –24 February, 27 February, 3 March	3.24	71.6%	13.2%
	4 March –13 March	4 March, 7 March, 11 March, 12 March, 13 March	4.09	90.4%	11.0%
	14 March –23 March	14 March, 15 March, 17 March, 19 March, 20 March	3.76	83.2%	7.6%
	24 March –2 April	24 March, 28 March	4.32	95.5%	5.8%

The second storm event we assessed was Cyclone Hudhud in Visakhapatnam, India. The dates of the pre-storm DNB images are listed in Table 8. Because the cloud cover was always high during that period, the 8-day MODIS reflectance data were affected by the cloud and did not reflect the true surface reflectance. Therefore, we removed the lunar contaminated DNB images (3 and 8 October). Figure 7 shows the pre- and post-storm averaging composite DNB images and the PNL image. Using the Mann-Whitney U-test, the difference between the pre-and post-earthquake DNB images was statistically significant at *p* < 0.001.

Table 8. The dates and cloud coverages of pre- and post-storm DNB images of the Cyclone Hudhud.

	Pre-Storm			Post-Storm			
Date	27 September	28 September	29 September	14 October	15 October	16 October	19 October
Days Before (After) the Disaster	15	14	13	2	3	4	7
Cloud Coverage (%)	15.6	6.6	0.0	19.8	4.9	8.6	1.2

A visual observation of the images showed that the scope and intensity of light reduced substantially after the cyclone. A pixel-by-pixel comparison showed that 695.3 km^2 of the area became darker, 11.8 km^2 became brighter, and 3.9 km^2 remained unchanged after the cyclone. The average radiance of the pre- and post-storm DNB were 7.8 nW·cm^{-2}·sr^{-1} and 2.4 nW·cm^{-2}·sr^{-1}, respectively. The PNL for the whole study area was 30.8%. To test whether the linear regression model derived from the example of Hurricane Maria (Figure 6) could be used to estimate the power outage in other cases, we applied the model to Cyclone Hudhud. The $P_{nopower}$ after Cyclone Hudhud was estimated to be 77.6%, which was in good agreement with the reported 20% or so power supply restoration work that was completed (that is, 80% of the power supply was not restored) by 16 October [77].
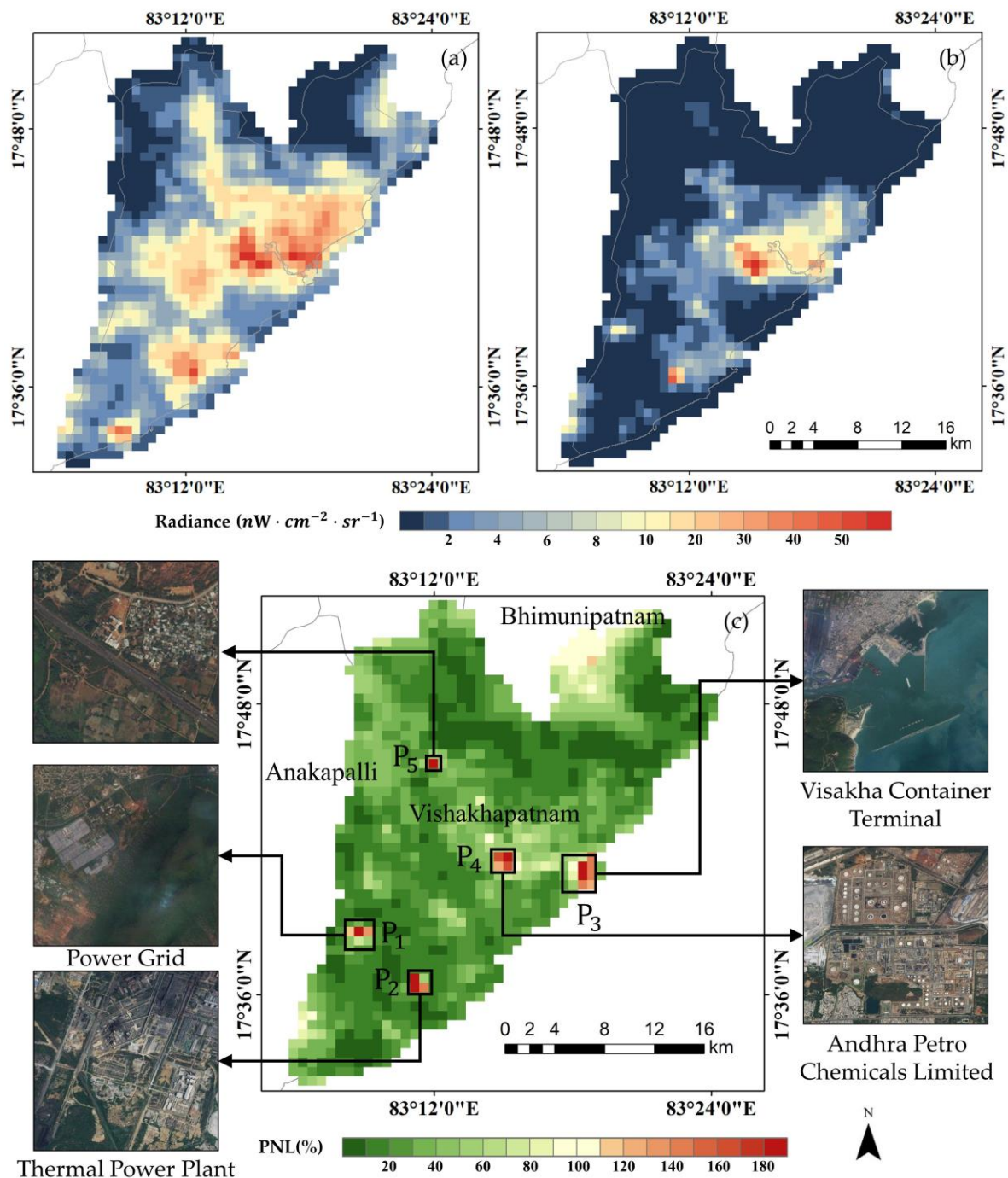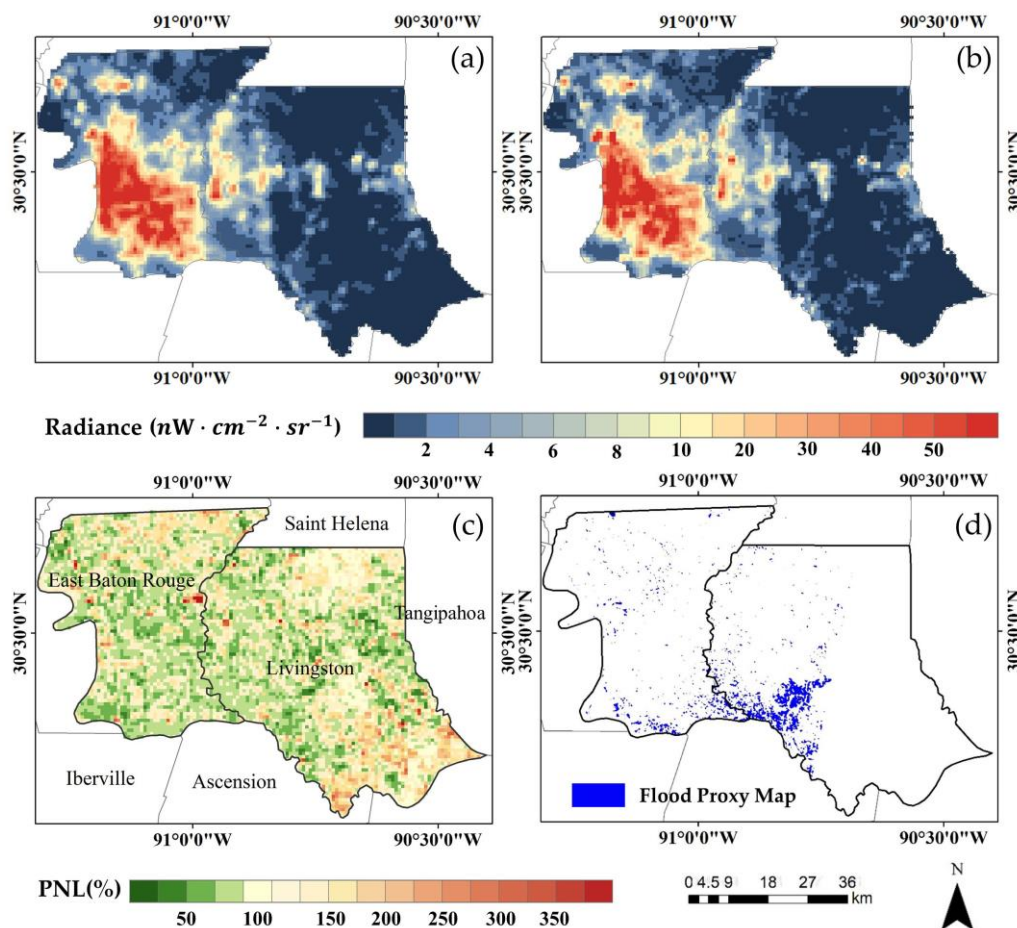
Figure 7. (**a**) The pre- and (**b**) post-storm averaging composite DNB images, (**c**) PNL image and Bing satellite images for the brighter region of Cyclone Hudhud.

However, there were also some places showing an increase in light after the cyclone. We identified these locations as Points of Interest (POIs) in the Bing high-resolution satellite map (Figure 7c, P_1–P_5). P_1 to P_4 are industrial sites (Power Grid, Thermal Power Plant, Petro Chemicals Limited, and Container Terminal), so the increase in light is attributable to the increased production of support power restoration. However, we did not note any abnormality at P_5, so we can only suspect this may have been related to fire or some transient lighting for facility repairs.

3.3. Floods

For the Louisiana flood in the U.S., because the cloud cover was heavy every day of the 10 days following the flood, the available images during that period could not cover the whole study area. Therefore, we chose the first three images covered the whole study area as the post-flood images (Table 9). Figure 8a–c show pre- and post-flood averaging composite DNB images and the PNL image. Figure 9d shows the Flood Proxy Map produced by ARIA on 18 August. The patterns of pre- and post-flood images were almost the same through visual analysis. The mean radiances of pre- and post-flood image were 7.87 nW·cm^{-2}·sr^{-1} and 7.79 nW·cm^{-2}·sr^{-1}, respectively. The brighter pixels and darker pixels were intertwined, with an area size of 2004.2 km^2 and 1891.7 km^2, respectively. The *p*-value of the Mann-Whitney U-test was 0.514, which indicated that the difference between the pre-and post-flood DNB images was not statistically significant at a 95% confidence interval. This is probably because the images used were captured 10 days after the flood and, in most areas, the power supply had been restored by then [78]. Furthermore, by comparing the FPM with the NTL map, we observed that the flood water was mainly located in areas with dim light. The light changes caused by the flood damage may not have been noticeable enough to be captured by NTL. Therefore, the NTL data were not useful in this case.

Figure 8. (**a**) The pre- and (**b**) post-flood averaging composite DNB images, (**c**) the PNL image, and (**d**) the Flood Proxy Map (FPM) of the Louisiana flood.

Table 9. The dates and cloud coverages of pre- and post-flood DNB images of the Louisiana Flood.

	Pre-Flood							Post-Flood		
Date	12 July	13 July	19 July	22 July	1 August	2 August	4 August	21 August	22 August	24 August
Days Before (After) the Disaster	30	29	23	20	10	9	7	10	11	13
Cloud Coverage (%)	0.0	0.0	9.0	0.0	19.9	0.0	5.6	22.7	21.3	0.0

For the Yulin flood in the Suide district in China, the dates and cloud coverages of pre- and post-flood DNB images are shown in Table 10. Pre- and post-flood averaging composite DNB images and the PNL image are shown in Figure 9a–c, respectively. The difference between the pre-and post-flood DNB images was statistically significant (Mann-Whitney U-test, $p < 0.001$).

Table 10. The dates and cloud coverages of pre- and post-flood DNB images of the Yulin Flood.

|	Pre-Flood				Post-Flood		
Date	27 June	29 June	1 July	17 July	30 July	31 July	2 August
Days Before (After) the Disaster	29	27	24	8	4	5	7
Cloud Coverage (%)	12.7	0.0	1.2	0.7	0.0	0.5	0.0
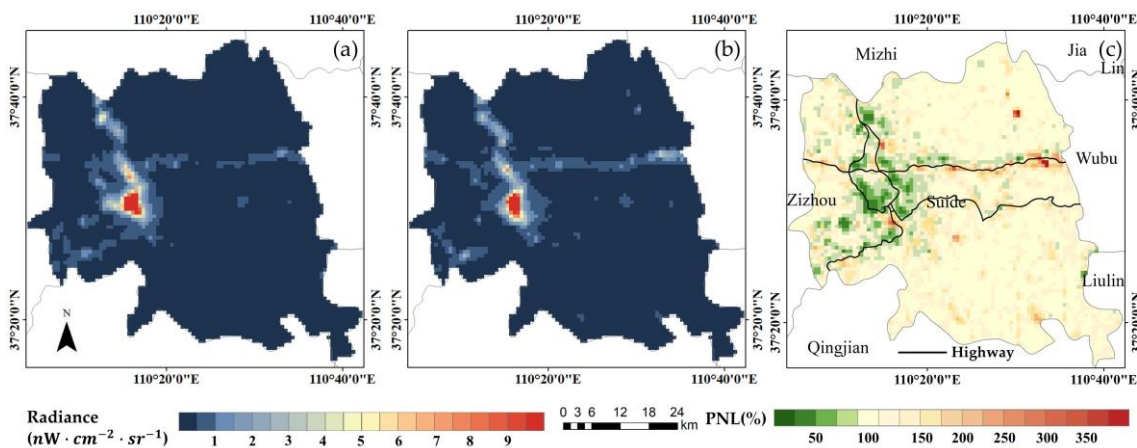
Figure 9. (**a**) The pre- and (**b**) post-flood averaging composite DNB images, and (**c**) the PNL image of the Yulin Flood.

Comparing the PNL image with the land cover map (Figure 1f), most of the urban areas became darker, which was consistent with the news report that the main county had undergone a large area of power outage [79]. It was reported that 194 houses collapsed during the flood [58]. As the number of housing collapses was relatively small, the main explanation for the light decrease could be due to power outages. Apart from the darker areas, there were still some pixels that became brighter, most of which were located along highways (Figure 9c of the highways). As all of the highways were seriously damaged by the flood [57], the brighter areas are probably attributable to the presence of rescue vehicles at night and the road repair work.

3.4. Impact of Clouds on Assessing Natural Disasters

Floods and storms are often accompanied by clouds that seriously affect the amount of data available. Figure 10 displays the percentage of cloud coverage for the 10 days from the beginning of the disastrous events that we analyzed. The percentage of cloud coverage was generally higher after storms and floods. For instance, the average cloud coverage rate for 10 days after Hurricane Maria in Puerto Rico was 85.0%. Under such high cloud coverage, the nighttime light changes could not be

detected by DNB. Subsequently, the usefulness of DNB in assessing the impact of this type of natural disaster would be limited.
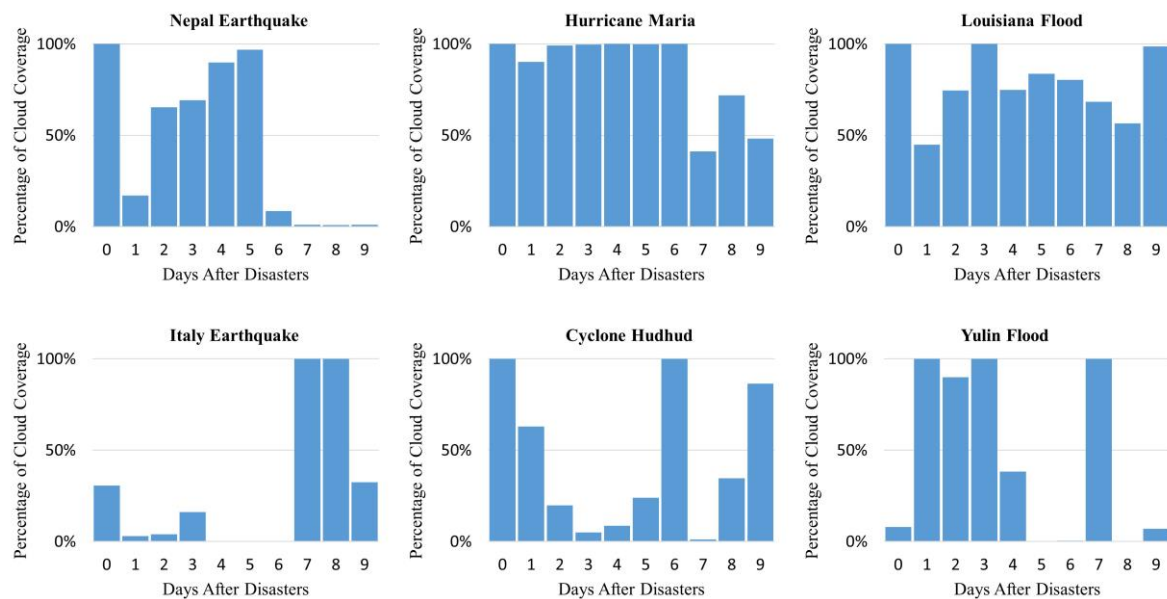
Figure 10. The percentage of cloud coverage in the study areas 10 days after each disaster.

4. Discussion

A natural disaster may cause damage to buildings and infrastructure, power outages, and impact human activities. All of these are expressed as a reduction in light intensity and can be identified in DNB images. Although the causes of light reduction cannot be revealed by DNB, which tend to differ for different types of disasters in different regions, our analyses showed that NPP-VIIRS DNB daily data can be used to assess the impact of various natural disasters, including earthquakes, storms, and floods. However, there are limitations due to the cloud coverage and influences by other human activities. Table 11 summarizes the applications of and major challenges encountered when using this type of data.

Earthquakes are one of the most destructive hazards that can cause large-scale building collapse and power outages. The overall accuracy, TRP, FPR and standard Kappa of using NTL to detect damage due to earthquakes were estimated to be 75.5%, 35.9%, 8.9%, and 0.31, respectively, in the Gorkha Nepal Earthquake. Previous research [41] used VIIRS NCC nighttime light to detect damage caused by three earthquakes with estimated overall accuracies of 75.0%, 68.4%, and 14.9%. Our result concurs with the highest accuracy of these three cases. According to the confusion matrices in their study, the standard Kappas would be close to 0, which is lower than our results. The TPRs would be 100%, 76.5%, and 14.9%, two of which would be higher than our results. The accuracy of using NTL to estimate the damage caused by earthquakes is not high due to a number of reasons, including the light from rescue activities that seriously affect the accuracy, and power outages that resulted in darkness from undamaged buildings as well. The situation is different under storm and flood events. For floods, variables that can influence building damage include the nature of the flood (such as water level, flood duration, and flow velocity) and the building properties (such as building structure and building quality) [80]. In urban areas where building structures are generally strong, floods would only destroy individual buildings along rivers. This is similar to storms during which only small numbers of individual buildings of poor quality are affected. Therefore, a decrease in the light in urban areas after floods or storms is likely due to power outages rather than building collapse. In the case of Hurricane Maria, we found a linear relationship between PNL and the power outage rate with an R^2 of 0.94. The linear regression model was further tested by applying it to the example of Cyclone Hudhud. The result showed that the estimated power outage rate was in good agreement with the reported

power outage rate. Previous research [37] used DNB data to detect power outages after Hurricane Sandy and found that the light outage percentages (defined as $LO_{DNB} = (1 - Rad_{post}/Rad_{pre})$) were in good agreement with the reported power outage rates, which further confirms the linear relationship between PNL and power outage rate. DNB would be more applicable in urban and developed rural areas that have a relatively high normal nighttime light intensity. In mountainous areas or small villages where residential properties are sparsely distributed and infrastructure and business are undeveloped, there is not much light at night even during normal times. The changes in light after disasters would be too small to be detected by satellite. For example, landslides are severe disasters that can cause large areas with buildings to be submerged. The 2017 Mocoa Colombia landslide buried large portions of Mocoa in several feet of mud and caused 329 deaths, 332 injuries, and 70 missing people [81]. However, the average DNB values before and after the landslide were both less than $0.2 \ nW \cdot cm^{-2} \cdot sr^{-1}$, which was almost no difference. As the DNB of an area with no light could be larger than $0.5 \ nW \cdot cm^{-2} \cdot sr^{-1}$ [67], these DNB data cannot be used to assess the impact of landslides.

Table 11. The applications and challenges of using DNB daily observations in disaster assessments.

Disaster Type	Event	Application	Validation Data	Validation Results	Challenges
Earthquake	Gorkha Nepal Earthquake	Identify damaged areas	DPM	Overall accuracy = 75.5% TPR = 35.9% FPR = 8.9% $K_{standard} = 0.31$ $K_{quantity} = 0.82$ $K_{location} = 0.46$	Rescue and repair activities produced extra lights
	Central Italy Earthquake	None	DPM	Overall accuracy = 90.2% TPR = 12.5% FPR = 9.0% $K_{standard} = 0.01$ $K_{quantity} = 0.84$ $K_{location} = 0.04$	Rescue and repair activities produced extra lights
Storm	Hurricane Maria	Detect power outages	DPM, and $P_{nopower}$ published by CESER in the U.S.	Strong correlation between the PNL and $P_{nopower}$ ($R^2 = 0.94$)	Cloud
	Tropical Cyclone Hudhud	Detect power outages	Power outage rate in news reports	The estimated $P_{nopower}$ of 77.6% was in good agreement with the report that 80% of the power supply was not restored.	Cloud
Flood	Louisiana Flood	None	FPM and news reports	Mann-Whitney U-test indicates that the difference between pre- and post-flood images is not statistically significant	Cloud
	Yulin Flood	Detect power outages	None	None	Increased rescue vehicles and repair activities brought extra lights

When faced with the same types of disasters, the changing pattern of NTL would be different due to the different socioeconomic statuses of the region. Take earthquakes as an example: for densely populated central urban areas, the normal NTL radiance value is very high. When an earthquake causes housing collapses and infrastructure damage, the light loss always becomes obvious. Under these circumstances, the impact of rescue lights is relatively minimal and NTL can be used to detect the affected area [39]. In contrast, the normal NTL for a sparsely populated village is low and rescue lights can be brighter than the normal NTL. Therefore, rescue lights would greatly affect the detection of damage.

By comparing the differences between NTL changes and the DPMs from the SAR data in the Gorkha Nepal Earthquake, Central Italy Earthquake, and Hurricane Maria, we noticed that the NTL satellite data directly recorded the light created by humans, whereas SAR data only reflect physical damage to the land surface. Therefore, the detected damage using SAR data may also include mountain deformations and other natural landform changes; the data do not directly reflect the impact on humans. NTL can directly reflect how humans are affected by natural disasters. However, the effect detected by NTL is complex and can include building damage, power outages, as well as human activities after the disaster, such as rescue work and changes to the number of vehicles on the road. The light sources cannot be distinguished by NTL itself. Therefore, using NTL to detect damage or power outages would be affected by other human activities like rescue activities and changes in traffic.

The major limitation of using DNB to assess the impact by natural disasters is cloud cover. Disasters like floods and storms are always accompanied by heavy rainfall and massive cloud coverage. Generally, the most serious power outages occurred immediately after the disaster. It is difficult to detect short-term light outages if the lost power is recovered a few days after the disaster because of heavy cloud coverage.

There are also some uncertainties when using the DNB data to assess the impact of natural disasters. Firstly, water brought by storms and floods can lead to changes in surface reflectance [82], which causes the surface to reflect less light. Secondly, the DNB data do not apply atmospheric corrections. The atmosphere, especially aerosol, has a scattering effect on NTL and can blur the artificial light [69]. Such limitations need to be fully assessed and considered when using NTL data.

5. Conclusions

The availability of the NPP-VIIRS DNB daily data enabled the use nighttime light data for short-term disaster assessments. This study explored the ability to use DNB daily data by assessing three types of natural disasters including earthquakes, storms, and floods. A series of preprocessing procedures were used to ensure the high data quality and that the PNL images were generated to reflect DNB changes following six typical disaster events. The results showed that the overall accuracy and standard Kappa of using PNL to detect the damage after the Gorkha Nepal Earthquake were 75.5% and 0.31, respectively. However, it was not possible to use PNL to detect the damage after the Central Italy Earthquake because many areas became brighter. This differs from previous research [39,40]. During the power restoration period after Hurricane Maria, the PNL value was significantly correlated with the power outage rate (R^2 = 0.94), indicating that NTL can be used to track power recovery trends. In the Cyclone Hudhud event, the $P_{nopower}$ estimated by PNL was in good agreement with the reported power outage, which is consistent with the work by Cao et al. [37]. In the flood events, power outages were detected by NTL after the Yulin Flood, but were not be detected after the Louisiana Flood because of the long cloudy days. The usefulness of NTL and SAR data in analyzing the impact of earthquakes and storms was compared. NTL can directly reflect human activities but cannot distinguish the causes of light reduction. SAR can detect building damage but also reflects natural land deformation. The major limitation of using DNB to assess damage after earthquakes is the presence of rescue activities, which are also related to the socioeconomic situation of the region. For the assessment of disasters accompanied by precipitation such as storms and floods, the presence of cloud is the major challenge that needs to be overcome.

This study has some limitations. In the absence of accurate survey data for building damage and power outages, we used DMPs from SAR data and power outage rates from local news reports as alternatives to validate the results. However, there are limitations and noise in these data, which lead to errors in the validation accuracy. Further validation of the assessments can be achieved as more accurate data on building damage and power outages become available. Given that the NTL and SAR data reflect different aspects of the impacts of natural disasters on humans, the combined use of these two data sources may improve the accuracy of damage detection and the assessment after natural disasters, which can be explored in future work. NASA has published the Black Marble

NTL daily data that offer cloud-free, atmospheric-, terrain-, vegetation-, snow-, lunar-, and stray light-corrected VIIRS DNB radiance [83]. Future work can evaluate the usefulness of this product to assess different disasters.

References

1. Soonee, S.; Narasimhan, S.; Nallarasan, N.; Rathour, H.K.; Yadav, G.; Bhan, S.; Mali, R. Impact of very severe cyclone 'hudhud'on power system operation. In Proceedings of the 2015 Annual IEEE India Conference (INDICON), New Delhi, India, 17–20 December 2015; pp. 1–5. [CrossRef]

2. Okamura, M.; Bhandary, N.P.; Mori, S.; Marasini, N.; Hazarika, H. Report on a reconnaissance survey of damage in Kathmandu caused by the 2015 Gorkha Nepal earthquake. *Soils Found.* **2015**, *55*, 1015–1029. [CrossRef]

3. Klemas, V. Remote sensing of floods and flood-prone areas: An overview. *J. Coast. Res.* **2015**, *314*, 1005–1013. [CrossRef]

4. Dell'Acqua, F.; Gamba, P. Remote sensing and earthquake damage assessment: Experiences, limits, and perspectives. *Proc. IEEE* **2012**, *100*, 2876–2890. [CrossRef]

5. Dell'Acqua, F.; Bignami, C.; Chini, M.; Lisini, G.; Polli, D.A.; Stramondo, S. Earthquake damages rapid mapping by satellite remote sensing data: L'aquila April 6th, 2009 event. *IEEE J. Sel. Top. Appl. Earth Obs. Remote. Sens.* **2011**, *4*, 935–943. [CrossRef]

6. Li, S.; Sun, D.; Goldberg, M.D.; Sjoberg, B.; Santek, D.; Hoffman, J.P.; DeWeese, M.; Restrepo, P.; Lindsey, S.; Holloway, E. Automatic near real-time flood detection using Suomi-NPP/VIIRS data. *Remote. Sens. Environ.* **2018**, *204*, 672–689. [CrossRef]

7. Elvidge, C.D.; Baugh, K.E.; Kihn, E.A.; Kroehl, H.W.; Davis, E.R. Mapping city lights with nighttime data from the DMSP operational linescan system. *Photogramm. Eng. Remote. Sens.* **1997**, *63*, 727–734.

8. Miller, S.D.; Straka, W.; Mills, S.P.; Elvidge, C.D.; Lee, T.F.; Solbrig, J.; Walther, A.; Heidinger, A.K.; Weiss, S.C. Illuminating the capabilities of the Suomi national polar-orbiting partnership (NPP) visible infrared imaging radiometer suite (VIIRS) day/night band. *Remote. Sens.* **2013**, *5*, 6717–6766. [CrossRef]

9. Elvidge, C.D.; Cinzano, P.; Pettit, D.; Arvesen, J.; Sutton, P.; Small, C.; Nemani, R.; Longcore, T.; Rich, C.; Safran, J. The nightsat mission concept. *Int. J. Remote. Sens.* **2007**, *28*, 2645–2670. [CrossRef]

10. Elvidge, C.D.; Baugh, K.; Zhizhin, M.; Hsu, F.C.; Ghosh, T. VIIRS night-time lights. *Int. J. Remote. Sens.* **2017**, *38*, 5860–5879. [CrossRef]

11. Liao, L.B.; Weiss, S.; Mills, S.; Hauss, B. Suomi NPP VIIRS day-night-band (DNB) on-orbit performance. *J. Geophys. Res. Atmos.* **2013**, *118*, 705–718. [CrossRef]

12. Shi, K.; Yu, B.; Huang, Y.; Hu, Y.; Yin, B.; Chen, Z.; Chen, L.; Wu, J. Evaluating the ability of NPP-VIIRS nighttime light data to estimate the gross domestic product and the electric power consumption of China at multiple scales: A comparison with dmsp-ols data. *Remote. Sens.* **2014**, *6*, 1705–1724. [CrossRef]

13. Doll, C.N.H.; Muller, J.P.; Morley, J.G. Mapping regional economic activity from night-time light satellite imagery. *Ecol. Econ.* **2006**, *57*, 75–92. [CrossRef]

14. Zhao, N.; Liu, Y.; Cao, G.; Samson, E.L.; Zhang, J. Forecasting China's gdp at the pixel level using nighttime lights time series and population images. *GISci. Remote. Sens.* **2017**, *54*, 407–425. [CrossRef]

15. Sutton, P.; Roberts, D.; Elvidge, C.; Baugh, K. Census from heaven: An estimate of the global human population using night-time satellite imagery. *Int. J. Remote. Sens.* **2001**, *22*, 3061–3076. [CrossRef]

16. Sutton, P.; Roberts, C.; Elvidge, C.; Meij, H. A comparison of nighttime satellite imagery and population density for the continental United States. *Photogramm. Eng. Remote. Sens.* **1997**, *63*, 1303–1313.

17. Elvidge, C.D.; Sutton, P.C.; Ghosh, T.; Tuttle, B.T.; Baugh, K.E.; Bhaduri, B.; Bright, E. A global poverty map derived from satellite data. *Comput. Geosci.* **2009**, *35*, 1652–1660. [CrossRef]

18. Yu, B.L.; Shi, K.F.; Hu, Y.J.; Huang, C.; Chen, Z.Q.; Wu, J.P. Poverty evaluation using NPP-VIIRS nighttime light composite data at the county level in China. *IEEE J. Sel. Top. Appl. Earth Obs. Remote. Sens.* **2015**, *8*, 1217–1229. [CrossRef]

19. Chand, T.R.K.; Badarinath, K.V.S.; Elvidge, C.D.; Tuttle, B.T. Spatial characterization of electrical power consumption patterns over India using temporal dmsp-ols night-time satellite data. *Int. J. Remote. Sens.* **2009**, *30*, 647–661. [CrossRef]

20. He, C.; Ma, Q.; Li, T.; Yang, Y.; Liu, Z. Spatiotemporal dynamics of electric power consumption in Chinese mainland from 1995 to 2008 modeled using DMSP/OLS stable nighttime lights data. *J. Geogr. Sci.* **2012**, *22*, 125–136. [CrossRef]

21. Shi, K.; Chen, Y.; Yu, B.; Xu, T.; Yang, C.; Li, L.; Huang, C.; Chen, Z.; Liu, R.; Wu, J. Detecting spatiotemporal dynamics of global electric power consumption using DMSP-OLS nighttime stable light data. *Appl. Energy* **2016**, *184*, 450–463. [CrossRef]

22. Shi, K.; Chen, Y.; Yu, B.; Xu, T.; Chen, Z.; Liu, R.; Li, L.; Wu, J. Modeling spatiotemporal CO_2 (carbon dioxide) emission dynamics in China from DMSP-OLS nighttime stable light data using panel data analysis. *Appl. Energy* **2016**, *168*, 523–533. [CrossRef]

23. Ghosh, T.; Elvidge, C.D.; Sutton, P.C.; Baugh, K.E.; Ziskin, D.; Tuttle, B.T. Creating a global grid of distributed fossil fuel CO_2 emissions from nighttime satellite imagery. *Energies* **2010**, *3*, 1895–1913. [CrossRef]

24. Chen, Z.Q.; Yu, B.L.; Hu, Y.J.; Huang, C.; Shi, K.F.; Wu, J.P. Estimating house vacancy rate in metropolitan areas using NPP-VIIRS nighttime light composite data. *IEEE J. Sel. Top. Appl. Earth Obs. Remote. Sens.* **2015**, *8*, 2188–2197. [CrossRef]

25. Hsu, F.-C.; Elvidge, C.D.; Matsuno, Y. Exploring and estimating in-use steel stocks in civil engineering and buildings from night-time lights. *Int. J. Remote. Sens.* **2013**, *34*, 490–504. [CrossRef]

26. Shi, K.; Yu, B.; Hu, Y.; Huang, C.; Chen, Y.; Huang, Y.; Chen, Z.; Wu, J. Modeling and mapping total freight traffic in China using NPP-VIIRS nighttime light composite data. *GISci. Remote. Sens.* **2015**, *52*, 274–289. [CrossRef]

27. Shi, K.; Chen, Y.; Yu, B.; Xu, T.; Li, L.; Huang, C.; Liu, R.; Chen, Z.; Wu, J. Urban expansion and agricultural land loss in China: A multiscale perspective. *Sustainability* **2016**, *8*, 790. [CrossRef]

28. Li, X.; Li, D. Can night-time light images play a role in evaluating the syrian crisis? *Int. J. Remote. Sens.* **2014**, *35*, 6648–6661. [CrossRef]

29. Li, X.; Zhang, R.; Huang, C.; Li, D. Detecting 2014 northern iraq insurgency using night-time light imagery. *Int. J. Remote. Sens.* **2015**, *36*, 3446–3458. [CrossRef]

30. Levin, N.; Ali, S.; Crandall, D. Utilizing remote sensing and big data to quantify conflict intensity: The Arab Spring as a case study. *Appl. Geogr.* **2018**, *94*, 1–17. [CrossRef]

31. Yu, B.; Tang, M.; Wu, Q.; Yang, C.; Deng, S.; Shi, K.; Peng, C.; Wu, J.; Chen, Z. Urban built-up area extraction from log-transformed NPP-VIIRS nighttime light composite data. *IEEE Geosci. Remote. Sens. Lett.* **2018**, 1–5. [CrossRef]

32. Shi, K.F.; Huang, C.; Yu, B.L.; Yin, B.; Huang, Y.X.; Wu, J.P. Evaluation of NPP-VIIRS night-time light composite data for extracting built-up urban areas. *Remote. Sens. Lett.* **2014**, *5*, 358–366. [CrossRef]

33. Huang, Q.X.; Yang, X.; Gao, B.; Yang, Y.; Zhao, Y.Y. Application of dmsp/ols nighttime light images: A meta-analysis and a systematic literature review. *Remote. Sens.* **2014**, *6*, 6844–6866. [CrossRef]

34. Elvidge, C.; Baugh, K.; Hobson, V.; Kihn, E.; Kroehl, H. Detection of fires and power outages using DMSP-OLS data. In *Remote Sensing Change Detection: Environmental Monitoring Methods and Applications*; Ross, S., Lunetta, C.D.E., Eds.; Taylor & Francis: London, UK, 1998; pp. 123–135.

35. Molthan, A.; Jedlovec, G. Satellite observations monitor outages from superstorm sandy. *Eos Trans. Am. Geophys. Union* **2013**, *94*, 53–54. [CrossRef]

36. Cole, T.; Wanik, D.; Molthan, A.; Román, M.; Griffin, R. Synergistic use of nighttime satellite data, electric utility infrastructure, and ambient population to improve power outage detections in urban areas. *Remote. Sens.* **2017**, *9*, 286. [CrossRef]

37. Cao, C.; Shao, X.; Uprety, S. Detecting light outages after severe storms using the S-NPP/VIIRS day/night band radiances. *IEEE Geosci. Remote. Sens. Lett.* **2013**, *10*, 1582–1586. [CrossRef]

38. Wang, Z.; Román, M.O.; Sun, Q.; Molthan, A.L.; Schultz, L.A.; Kalb, V.L. Monitoring disaster-related power outages using NASA black marble nighttime light product. *Int. Arch. Photogramm. Remote. Sens. Spat. Inf. Sci.* **2018**, *XLII-3*, 1853–1856. [CrossRef]

39. Kohiyama, M.; Hayashi, H.; Maki, N.; Higashida, M.; Kroehl, H.W.; Elvidge, C.D.; Hobson, V.R. Early damaged area estimation system using DMSP-OLS night-time imagery. *Int. J. Remote. Sens.* **2004**, *25*, 2015–2036. [CrossRef]

40. Hayashi, H.; Matsuoka, M.; Fujita, H. Use of DMSP-OLS images for early identification of impacted areas due to the 1999 Marmara earthquake disaster. In Proceedings of the 20th Asian Conference on Remote Sensing, Hong Kong, China, 22–25 November 1999; pp. 1291–1296.

41. Fan, X.; Nie, G.; Deng, Y.; An, J.; Zhou, J.; Li, H. Rapid detection of earthquake damage areas using VIIRS nearly constant contrast night-time light data. *Int. J. Remote. Sens.* **2018**. [CrossRef]

42. Roman, M.O.; Stokes, E.C. Holidays in lights: Tracking cultural patterns in demand for energy services. *Earth Future* **2015**, *3*, 182–205. [CrossRef] [PubMed]

43. Agnew, J.; Gillespie, T.W.; Gonzalez, J.; Min, B. Baghdad nights: Evaluating the US military 'surge'using nighttime light signatures. *Environ. Plan. A* **2008**, *40*, 2285–2295. [CrossRef]

44. Emergency Events Database. Available online: http://emdat.be/emdat_db/ (accessed on 26 June 2018).

45. Commission, N.P. *Nepal Earthquake 2015: Post Disaster Needs Assessment. Vol. A: Key Findings*; Government of Nepal, National Planning Commission: Kathmandu, Nepal, 2015.

46. Italy in Shock after Amatrice Earthquake: This Used to Be My Home. Available online: https://www.theguardian.com/world/2016/aug/24/italy-earthquake-rescue-teams-dig-through-rubble-as-death-toll-rises (accessed on 26 June 2018).

47. Amatrice (Italy) Earthquake Response. Available online: http://disastertechlab.org/2016/09/21/amatrice-italy-earthquake-response/ (accessed on 26 June 2018).

48. In Pictures: Hurricane Maria Pummels Puerto Rico. Available online: http://edition.cnn.com/interactive/2017/09/world/hurricane-maria-puerto-rico-cnnphotos/ (accessed on 26 June 2018).

49. Hurricane Maria Updates: In Puerto Rico, the Storm 'Destroyed US'. Available online: https://www.nytimes.com/2017/09/21/us/hurricane-maria-puerto-rico.html (accessed on 26 June 2018).

50. Hurricanes Nate, Maria, Irma, and Harvey Situation Reports. Available online: https://www.energy.gov/ceser/downloads/hurricanes-nate-maria-irma-and-harvey-situation-reports (accessed on 26 June 2018).

51. Hudhud: Another Damaging Bay of Bengal Storm. Available online: https://earthobservatory.nasa.gov/IOTD/view.php?id=84547 (accessed on 26 June 2018).

52. Cyclone Hudhud-Strategies and Lessons for Preparing Better & Strengthening Risk Resilience in Coastal Regions of India. Available online: https://ndma.gov.in/en/ndma-reports.html (accessed on 20 September 2018).

53. Cyclone Hudhud Path and Affected Area Map. Available online: http://www.mapsofindia.com/mapinnews/cyclone-hudhud/ (accessed on 26 June 2018).

54. August 2016 Record Flooding. Available online: https://www.weather.gov/lix/August2016flood (accessed on 26 June 2018).

55. Thousands Still without Power; Many Will Have to Wait until Water Recedes, Officials Say. Available online: http://www.theadvocate.com/baton_rouge/news/weather_traffic/article_57ef9db6-633c-11e6-b19a-d7be27b1784b.html (accessed on 26 June 2018).

56. Louisiana governor: 40K homes damaged by historic flooding, 11 killed. Available online: https://www.ctvnews.ca/world/louisiana-governor-40-000-homes-damaged-by-historic-flooding-11-killed-1.3030316 (accessed on 21 September 2018).

57. He, Y.; He, S.; Hu, Z.; Qin, Y.; Zhang, Y. The devastating 26 July 2017 floods in Yulin city, northern Shaanxi, China. *Geomat. Nat. Hazards Risk* **2017**, *9*, 70–78. [CrossRef]

58. The Flood in Suide, Shaanxi Province Have Affected 135,300 People and Caused Economic Losses of 2.265 Billion Yuan. Available online: http://www.jianzai.gov.cn//DRpublish/ztzl/0000000000025130.html (accessed on 26 June 2018).

59. NOAA Comprehensive Large Array-Data Stewardship System (CLASS). Available online: https://www.bou.class.noaa.gov/saa/products/welcome (accessed on 9 March 2018).

60.   NASA EARTHDATA powered by the Earth Observing System Data and Information System (EOSDIS). Available online: https://earthdata.nasa.gov/ (accessed on 9 March 2018).

61.   NASA Jet Propulsion Laboratory Advanced Rapid Imaging and Analysis (ARIA) Project for Natural Hazards. Available online: https://aria.jpl.nasa.gov/ (accessed on 9 March 2018).

62.   Open Street Map. Available online: https://www.openstreetmap.org (accessed on 9 March 2018).

63.   GLOBELAND30. Available online: http://globallandcover.com/GLC30Download/index.aspx (accessed on 9 March 2018).

64.   GADM maps and data. Available online: https://gadm.org/ (accessed on 9 March 2018).

65.   Bai, Y.; Cao, C.Y.; Shao, X. Assessment of scan-angle dependent radiometric bias of Suomi-NPP VIIRS day/night band from night light point source observations. In *Earth Observing Systems XX*; Butler, J.J., Xiong, X., Gu, X., Eds.; Spie-Int Soc Optical Engineering: Bellingham, 2015; Vol. 9607.

66.   Hillger, D.; Seaman, C.; Liang, C.; Miller, S.; Lindsey, D.; Kopp, T. Suomi NPP VIIRS imagery evaluation. *J. Geophys. Res. Atmos.* **2014**, *119*, 6440–6455. [CrossRef]

67.   Cao, C.Y.; Bai, Y. Quantitative analysis of VIIRS DNB nightlight point source for light power estimation and stability monitoring. *Remote. Sens.* **2014**, *6*, 11915–11935. [CrossRef]

68.   Miller, S.D.; Turner, R.E. A dynamic lunar spectral irradiance data set for NPOESS/VIIRS day/night band nighttime environmental applications. *IEEE Trans. Geosci. Remote. Sens.* **2009**, *47*, 2316–2329. [CrossRef]

69.   Johnson, R.S.; Zhang, J.; Hyer, E.J.; Miller, S.D.; Reid, J.S. Preliminary investigations toward nighttime aerosol optical depth retrievals from the VIIRS day/night band. *Atmos. Meas. Tech.* **2013**, *6*, 1245–1255. [CrossRef]

70.   Schueler, C.F.; Lee, T.F.; Miller, S.D. Viirs constant spatial-resolution advantages. *Int. J. Remote. Sens.* **2013**, *34*, 5761–5777. [CrossRef]

71.   Levin, N. The impact of seasonal changes on observed nighttime brightness from 2014 to 2015 monthly viirs dnb composites. *Remote. Sens. Environ.* **2017**, *193*, 150–164. [CrossRef]

72.   Nachar, N. The Mann-Whitney U: A test for assessing whether two independent samples come from the same distribution. *Tutor. Quant. Methods Psychol.* **2008**, *4*, 13–20. [CrossRef]

73.   Pontius, R.G. Quantification error versus location error in comparison of categorical maps. *Photogramm. Eng. Remote. Sens.* **2000**, *66*, 1011–1016.

74.   Nearly Half a Million in Nepal Are Displaced from Their Homes; More Than 5,000 Dead. Available online: https://www.pri.org/stories/2015-04-25/devastating-earthquake-leaves-more-thousand-dead-and-rising-nepal (accessed on 13 August 2018).

75.   Italy Earthquake: Death Toll Rises to 267, Nearly 400 Hospitalised, Authorities Say. Available online: http://www.abc.net.au/news/2016-08-26/italy-quake-death-toll-rises-to-267-nearly-400-hospitalised/7789868 (accessed on 13 August 2018).

76.   Aftershocks Damage Access Routes to Earthquake-Damaged Village. Available online: http://www.irishnews.com/news/worldnews/2016/08/27/news/aftershocks-damage-access-routes-to-earthquake-damaged-village-669348/ (accessed on 13 August 2018).

77.   Hudhud Aftermath: Priority to Restore Power, Supply Essentials. Available online: http://www.thehindu.com/news/cities/Visakhapatnam/hudhud-aftermath-priority-to-restore-power-supply-essentials/article6503909.ece (accessed on 26 June 2018).

78.   Entergy Restores Power to Majority of Customers after Historic Flooding. Available online: http://www.tdworld.com/electric-utility-operations/entergy-restores-power-majority-customers-after-historic-flooding (accessed on 26 June 2018).

79.   A Dam Failure Warning Was Issued in Yulin, Shaanxi: The Reservoir Overflows and the Residents Need to Evacuate Immediately. Available online: http://news.china.com/domestic/945/20170726/31007133.html (accessed on 26 June 2018).

80.   Thieken, A.H.; Müller, M.; Kreibich, H.; Merz, B. Flood damage and influencing factors: New insights from the august 2002 flood in germany. *Water Resour. Res.* **2005**, *41*. [CrossRef]

81.   Colombia Landslide Leaves at Least 254 Dead and Hundreds Missing. Available online: https://www.theguardian.com/world/2017/apr/01/colombia-landslide-mocoa-putumayo-heavy-rains (accessed on 26 June 2018).

82. Kerekes, J.P.; Strackerjan, K.; Salvaggio, C. Spectral reflectance and emissivity of man-made surfaces contaminated with environmental effects. *Opt. Eng.* **2008**, *47*, 106201. [CrossRef]

83. Román, M.O.; Wang, Z.; Sun, Q.; Kalb, V.; Miller, S.D.; Molthan, A.; Schultz, L.; Bell, J.; Stokes, E.C.; Pandey, B.; et al. Nasa's black marble nighttime lights product suite. *Remote. Sens. Environ.* **2018**, *210*, 113–143. [CrossRef]